2005

Modelling infragravity motions on a rip-channel beach

Reniers, A.J.H.M.

Coastal Engineering, 2005
http://hdl.handle.net/10945/45798

ARTICLE IN PRESS

Available online at www.sciencedirect.com

SCIENCE DIRECT®

Coastal Engineering xx (2005) xxx – xxx

Coastal Engineering
An International Journal for Coastal, Harbour and Offshore Engineers

www.elsevier.com/locate/coastaleng

Modelling infragravity motions on a rip-channel beach

A.J.H.M. Reniers [a,*], J.H. MacMahan [b], E.B. Thornton [c], T.P. Stanton [c]

[a] Delft University of Technology, Department of Civil Engineering and Geosciences, Delft, The Netherlands
[b] Center for Applied Coastal Research, University of Delaware, Ocean Engineering Laboratory, Newark, USA
[c] Naval Postgraduate School, Oceanography Department, Monterey, USA

Abstract

A non-linear shallow water wave model operating on the time-scale of wave groups is compared with measurements of infragravity motions on a rip-channel beach to verify the model concepts and assess the model performance. The measurements were obtained during the RIP-current EXperiment (RIPEX) in concert with the Steep Beach Experiment (SBE) performed at Sand City, Monterey Bay, CA, during the spring of 2001. The nearshore bathymetry was made up of shore-connected shoals incised by relatively narrow rip-channels spaced approximately 125 m apart. The comparison considers a 20-day period during which significant changes in both the offshore wave climate and nearshore bathymetry occurred. The temporal variation in infragravity conditions during the experiment is strong, with computational results typically explaining 70% to 80% of the observed infragravity motions within the nearshore. In contrast to the temporal variation, the alongshore spatial variation in infragravity intensity during the experiment is generally weak, even though the underlying bathymetry shows strong depth variations. Model computations suggest preferential coupling between the computed edge wave motions and the quasi-periodic bathymetry is present, a prerequisite for strong spatial variability. However, the infragravity field is dominated by cross-shore infragravity motions, which are only weakly coupled to the quasi-periodic bathymetry, resulting in a weak alongshore variability of the total infragravity motions.

Keywords: Infragravity waves; Rip-channels; Edge waves; Numerical modelling; Field measurements; Alongshore variability; Bathymetric coupling

1. Introduction

Infragravity waves with periods between 20 s to 5 min are generally associated with the groupiness, or the beat, of the incident waves (Munk, 1949; Tucker, 1950). The infragravity wave field is typically made up of both leaky, i.e. infragravity waves that radiate away from the surfzone, and trapped long waves (edge waves) that cannot escape from the shoreline due to strong refraction. Previous measurements (Suhayda, 1974; Huntley, 1976; Holman, 1981; Wright et al., 1982; Guza and Thornton, 1985, among others) have shown the increased contribution of infragravity motions to the total gravity wave spectrum with decreasing water depth. This effect is associated with the wave-breaking induced saturation of the incident waves, whereas the infragravity waves continue to shoal without breaking, consequently their relative contribution increases rapidly as the shoreline is approached and can reach energy levels significantly higher than the incident wind waves (Wright et al., 1982; Guza and Thornton, 1985). Infragravity waves are therefore important in wave overtopping and run-up on dikes and dunes (Van Gent, 2001) as well as dune erosion (Overton and Fischer, 1988). The related safety of the hinterland calls for reliable model predictions of infragravity waves under a wide range of conditions.

So far, comparisons of computed infragravity conditions with field data have been limited. List (1992) compared his 1D-model with data obtained at Duck, North Carolina to explain the release of bound long waves within the surfzone. Reniers et al. (2002) used a linear 1D spectral model and measurement-data from the DELILAH field experiment (Thornton and Kim, 1993) and obtained favorable comparisons for the infragravity conditions. A subset of that data was utilized by Van Dongeren et al. (2003) in a comparison with a 2D non-linear model that showed the beach at the time of the DELILAH experiment could be considered as being alongshore uniform for the infragravity conditions.

The presence of alongshore variability in the bathymetry is expected to be important in view of the potential coupling between infragravity conditions and the underlying bathymetry

* Corresponding author.
E-mail address: a.j.h.m.reniers@citg.tudelft.nl (A.J.H.M. Reniers).

0378-3839/$ - see front matter © 2005 Elsevier B.V. All rights reserved.
doi:10.1016/j.coastaleng.2005.10.010

(Bowen and Inman, 1971; Holman and Bowen, 1982; Chen and Guza, 1998; 1999), resulting in a strongly inhomogeneous infragravity field. However, measurements of infragravity motions often give little idea about the alongshore variation of infragravity conditions due to the fact that the measurements are isolated (Elgar et al., 1992; Okihiro et al., 1992), or restricted to the cross-shore (Huntley, 1976; Guza and Thornton, 1985; Ruessink, 1998a), or performed at what would be considered an alongshore uniform beach (Huntley et al., 1981; Oltman-Shay and Guza, 1987; Herbers et al., 1995). Most notably, measurements at a number of beaches in South-Eastern Australia suggested the expected coupling between (complex) nearshore bathymetry and the infragravity (edge-)wave field (Wright et al., 1979), due to the presence of preferentially forced infragravity frequencies in the measured surface elevation and velocity spectra. Although these experiments were rich in morphological contrast, the number of instruments was typically limited (five or less within the nearshore) and information on the adjacent bathymetry, a requirement for modelling efforts, was sparse.

The main objective of this paper is to verify the numerical modelling of infragravity conditions on an alongshore variable beach. Measurements of infragravity motions during the RIP-current field EXperiment (RIPEX) in concert with the Steep Beach Experiment (SBE) at Sand City, Monterey Bay, are used for comparison with the numerical model results. The bathymetry was repeatedly surveyed to produce a high resolution bathymetry time series. During most of the year, the beach at this location consists of shore-connected shoals incised by narrow rip-channels with an alongshore spacing of 100–250 m. A detailed description of the experiment and the analysis of the measured infragravity motions is given in the paper by MacMahan et al. (2004a).

The model approach, briefly described in Section 2, allows for directional spreading in the incident waves and the generation and propagation of leaky and trapped infragravity waves over an arbitrary 2D bathymetry utilizing the non-linear shallow water equations in conjunction with a wave driver that operates on the time-scale of wave groups (Reniers et al., 2004, denoted RRT04 hereafter). The model–measurement comparisons, spanning a period of 20 days, are described in Section 3. Comparisons focus on the temporal and spatial variation of the infragravity velocities and wave heights. During this exercise both the wave-breaking parameters and bottom friction coefficients are kept constant. The effects of the alongshore variability in the bathymetry are discussed in Section 4. Conclusions with respect to the model performance are given in Section 5.

2. Model description

A brief model description is given below. For a more detailed model description refer to RRT04. The numerical model utilized is an extended research version of Delft3D. Delft3D, developed by WL|Delft Hydraulics, is a comprehensive numerical model suite, which includes a wave driver, hydrodynamic flow, sediment transport, and morphologic response modules. The extensions considered in this paper are a more sophisticated wave driver to account for the effects of wave groupiness and the inclusion of surface rollers to describe wave breaking. Morphodynamic effects (RRT04) are not discussed in this paper, and model computations are performed over the measured fixed beds.

The wave driver considers the modulated wave energy associated with wave groups made up of the directionally spread spectral sea and swell components, to generate infragravity waves through triad interactions. A single summation random phase method (see Van Dongeren et al., 2003, for details) is utilized to generate surface elevation time series from the measured energy density frequency-direction wave spectrum, $E(f, \theta)$, at the offshore boundary. Applying a Hilbert transform to the surface elevation time series in combination with a low-pass filter yields the spatially and temporally modulated wave energy used as input for the wave driver. This energy, on the wave-group scale, is then propagated shoreward and released at wave breaking where it is first transferred to roller energy prior to dissipation, causing a spatial lag between the location of wave breaking and the actual dissipation (Nairn et al., 1990). Wave diffraction and wave–current interaction are neglected at present.

The temporal and spatial variation of the wave and roller energy are then used to calculate the radiation stresses. The mean and infragravity motions are solved using non-linear shallow water equations forced by the divergence of these radiation stresses to phase-resolve bound and free infragravity waves, both trapped (edge waves) and leaky.

The combined wave- and current bottom shear stresses are computed with the parameterization given by Soulsby et al. (1993) of the friction formulation of Fredsoe (1984). The parameterization is based on the current- and wave-only bed shear stress formulations and the angle between waves and flow. The drag coefficient, C_D, in the current shear stress is computed with Manning's formulation:

$$C_D = \frac{h^{\frac{1}{6}}}{n_m} \tag{1}$$

with n_m Manning's coefficient and h the local water depth. The wave friction factor in the wave-only bed shear stress is obtained with Swart's (1974) formulation.

Given the tidal variation, parts of the beach will become dry at low tide. To account for this, a procedure is applied that removes grid points during the falling of the tide and adds them during its rise (Stelling et al., 1986). If the water level at a velocity point gets below a threshold, the velocity point is set dry. If the water level becomes twice the threshold value, the point becomes wet again. A value of 0.2 m for the threshold is used in the computations.

3. Comparison with measurements

3.1. Introduction

During RIPEX-SBE, the offshore wave climate, measured with a directional Wave-Rider buoy 650 m offshore in a depth

of 17 m, showed considerable variation in both wave height and wave period (Fig. 1). Long period swell with wave periods in excess of 10 s and significant wave heights close to 3 m occurred during a storm event around yearday 122. More modest storm conditions occurred around yearday 130 and again around yearday 138.

In contrast to the large variability in wave height, the mean wave incidence angle shows little variation with a predominant direction normal to shore. This lack in directional variation is associated with the sheltering effects of the bay (MacMahan et al., 2005), which filters out most directional spreading (panel d of Fig. 1). During the times of the relatively few cases of local wind generated sea waves, the direction showed more variation. The occurrence of locally generated waves is also reflected in the mean period, which switches from predominantly swell periods to sea waves during these occasions. Tidal elevation data were obtained from the NOAA/NOS-wave gauge deployed near the Monterey harbour 2 km south of the experiment site.

The surveyed bathymetry during RIPEX-SBE, stretching 500 m in the alongshore and 250 m offshore, typically encompassed several rip-cell systems (left panel of Fig. 2). To mitigate effects at the (unknown) lateral boundaries, the computational domain is extended periodically approximately 300 m both up-coast and down-coast utilizing the measured bathymetry in the interior. Periodic boundary conditions are presently not available. Instead the infragravity waves traveling along the coast are reflected at the lateral boundaries. The nodal structure associated with these reflections disappears away from the side walls due to topographic scattering of the infragravity waves over the complex bathymetry resulting in smooth energy density spectra in the area of interest (i.e. at the measurement arrays) approximating conditions on an infinitely long beach. The lateral extensions result in a model domain of approximately 1100 m in the alongshore (a further increase of the alongshore domain length gave negligible differences in the computations). The cross-shore domain is 680 m, extending to the position of the wave buoy at 17 m water depth. The depth contours beyond 10 m water depth were obtained by a linear interpolation and are assumed to be alongshore uniform. Reflection of infragravity waves is imposed at the shoreline. At the offshore boundary, a Riemann condition is used to allow the leaky infragravity waves (generated in the surf zone) to leave the domain (Verboom and Slob, 1984). The alongshore grid spacing is 10 m, whereas the cross-shore grid spacing is spatially varying with finer grid-resolution of approximately 4 m within the surfzone (right panel of Fig. 2). The modelling time step is 2.4 s. No significant changes in the computational results occurred utilizing smaller grid-spacings and/or time steps.

The instruments utilized in the model–data comparisons comprised a cross-shore array traversing the shoal and an alongshore array covering a complete rip-cell system (left panel of Fig. 2). The measurements obtained with the cross-shore array are used to examine the transformation of sea/swell and infragravity waves across the shoal. To examine the effects of alongshore variations in the bathymetry, the alongshore array of six co-located pressure sensors and current meters is used.

The comparison considers the frequency integrated infragravity energy density expressed as the low frequency wave height, $H_{\mathrm{rms,lo}}$ and low frequency velocities $U_{\mathrm{rms,lo}}$ and $V_{\mathrm{rms,lo}}$. The comparisons are based on records with a length of 90 min, divided in Hanning-windowed subseries of 256 s, resulting in a frequency resolution, δf, of 0.0039 Hz with 41 degrees of

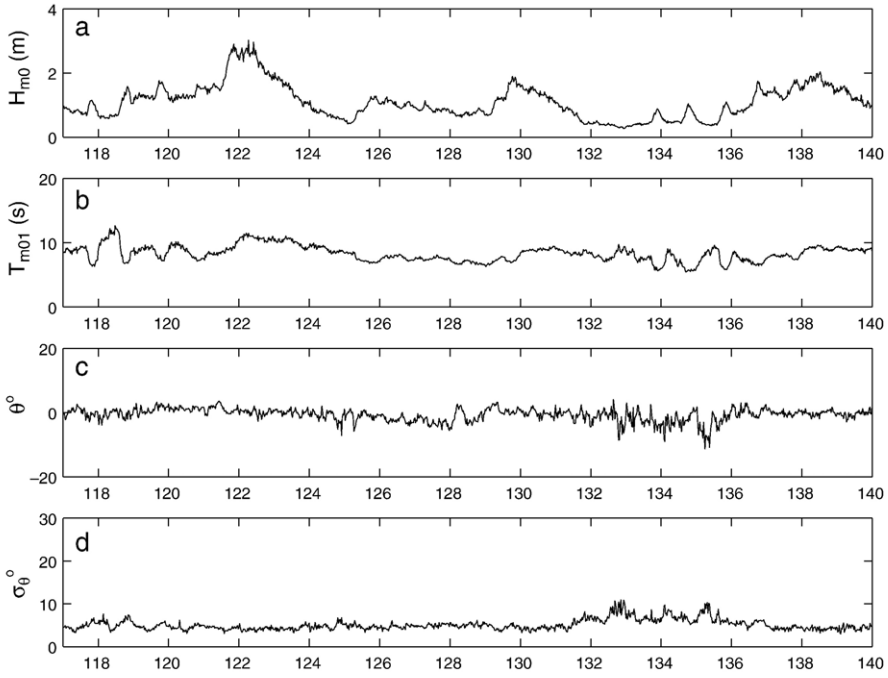

Fig. 1. Offshore conditions during the RIPEX-SBE experiment. Panel a: significant wave height. Panel b: mean period. Panel c: mean wave direction with respect to shore normal. Panel d: directional spreading of the incident waves.

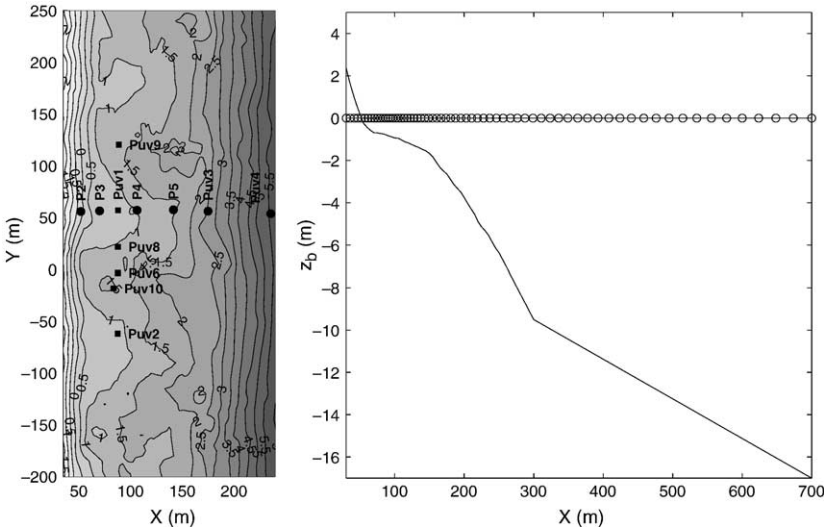

Fig. 2. Left panel: survey for yearday 117. Right panel: cross-shore grid-points (circles) with bottom profile at the cross-shore transect as a reference.

freedom, thus excluding very low frequency motions (MacMahan et al., 2004b), which will be presented elsewhere. A single computational record has a length of 30 min during which wave conditions are assumed to be stationary. The 90-min record of the model computations is then obtained by summing three consecutive half hours records. The modelled time-varying eulerian infragravity velocity and surface elevation, are spectrally integrated over the same low frequency range as the measurements to avoid possible contamination of higher frequency motions in the numerical solution.

The local measured sea/swell wave height, $H_{\mathrm{rms,hi}}$, is obtained by transforming the measured pressure spectrum to surface elevation using linear wave theory with a low frequency cut-off, f_{l}, at 0.04 Hz and a high frequency cut-off frequency, f_{h}, at 0.35 Hz (see MacMahan et al., 2004a).

The low frequency wave period is computed by:

$$T_{\mathrm{m01,lo}} = \frac{\int_{\delta f}^{f_l} E(f)df}{\int_{\delta f}^{f_l} fE(f)df} \tag{2}$$

where E is the energy density and f the frequency.

Model computations are performed with constant values for both the roller dissipation parameter, $\beta = 0.1$ (RRT04 Eq. (5)), representing the slope of the breaking wave and Manning's friction parameter, $n_{\mathrm{m}} = 0.02$. Both bottom friction and roller dissipation are known to have an important effect on the resulting infragravity intensity (Reniers et al., 2002). However, their effect is predominantly an amplification or damping of the infragravity intensities throughout the domain, only numerically modifying the cross-shore structure. It is noted that these are not free parameters as they also affect the mean flow and cannot be varied at will. A sensitivity analysis with respect to the roller dissipation and bottom friction was performed by Reniers et al. (2002) and will not be pursued here.

The total duration of RIPEX-SBE was 42 days of which 20 days have been selected for the model–measurement comparison based on the maximum availability of relevant measurement data. The bathymetry was surveyed four times within the 20-day period, showing significant changes in between the surveys (MacMahan et al., 2005). The surveys are therefore representative for a shorter period than the actual survey interval, and significant differences between the computational bathymetry and the real bathymetry can be present at times. This is especially true for the period during and after the main storm event at yearday 122 when rapid evolution of the bar system can be expected. Surveys closest to each modelling yearday are used to construct the computational bathymetry, with the exception of the days after the main storm event in which the first post-storm survey is used.

3.2. Cross-shore array comparison

As mentioned previously changes in the wave-group forcing are responsible for the generation of infragravity waves. Errors in the wave transformation will therefore result in errors in the computed infragravity results. The focus of the present paper is on the infragravity waves and not so much the wave transformation. To that end, the wave transformation has been optimized to give an accurate prediction of the wave height throughout the surf zone even though discrepancies can still occur, e.g. due to reflection of the incident swell waves. The present results were obtained with $n_{\mathrm{d}} = 10$, representing the irregularity of the incident wave field (Roelvink, 1993) and the wave breaking parameter $\gamma = 0.45$ (RRT04 Eq. (2)). Three parameters are introduced to evaluate the model predictions: a linear regression coefficient, a, of a regression line which is forced through the origin, a root mean square error, ε_{r}, defined as:

$$\varepsilon_{\mathrm{r}} = \sqrt{\frac{1}{N}\sum_{i=1}^{N}\left(G_{m,i} - G_{c,i}\right)^2} \tag{3}$$

and model skill given by (Gallagher et al., 1998):

$$\mathrm{skill} = 1 - \sqrt{\frac{\frac{1}{N}\sum_{i=1}^{N}\left(G_{m,i} - G_{c,i}\right)^2}{\frac{1}{N}\sum_{i=1}^{N}\left(G_{m,i}\right)^2}} \tag{4}$$

where G stands for the quantity to be evaluated with the subscripts m and c denoting measured and computed respectively, and N is the number of observations.

Starting at the most offshore sensor, Puv4 (Fig. 2), deployed in approximately 6 m water depth, the measured wave height (upper most panel of Fig. 3) shows strong similarity to the wave height at the offshore buoy (panel a of Fig. 1), indicating there is little wave breaking beyond the 6 m depth contour except at the peak of the storm around yearday 122. The computed wave transformation tracks the measurements for most of the time, though on average, the wave height is slightly overestimated. The next sensor, Puv3, was deployed in approximately 3 m water depth. Both computed and measured wave height show the effects of wave breaking during the storm events. Pressure sensor P5 was deployed in approximately 2 m water depth and subsequently subject to frequent wave breaking, which is also present in the computations. Pressure sensor P4 is located at a water depth of 1.5 m and exhibits strong tidal modulation of the incident wave height throughout the whole period. Similar behavior is observed at pressure sensor P3, deployed at a similar water depth as P4, but positioned closer to shore in line with the feeder channels (see Fig. 2). Computations of the incident wave height at these two sensors correspond well with the measurements. Close to the shoreline at P2, both computed and measured incident wave height drop to zero at some low tide stages at the start of the measurements. The overall root-mean-square error in the wave transformation was $O(10)$ cm with a skill of 0.85 (see Table 1) and a linear regression coefficient of 0.96.

Table 1
Root mean square error estimates, ε_r in (m), skill factors and linear regression coefficient, a, for high (columns 4–6) and low frequency wave transformation (columns 7–9) at the cross-shore array

Sensor	X (m)	Y (m)	ε_r(m)	Skill	a	ε_r(m)	Skill	a
Puv4	235.5	53.5	0.09	0.90	0.97	0.02	0.88	0.96
Puv3	175.0	56.2	0.11	0.87	1.00	0.03	0.85	0.98
P5	141.6	57.5	0.10	0.86	1.05	0.04	0.80	0.90
P4	106.5	57.0	0.08	0.84	0.91	0.04	0.82	0.99
P3	70.2	56.5	0.06	0.86	0.96	0.04	0.83	1.01
P2	52.1	55.7	0.09	0.77	0.85	0.07	0.82	1.01
Mean			0.09	0.85	0.96	0.04	0.83	0.98

The cross-shore transformation of the infragravity wave height is considered next (Fig. 4). At Puv4, the infragravity wave height, $H_{rms,lo}$, follows the trends of the incident wave height with maximums coinciding with the maximum incident wave heights. At Puv3, $H_{rms,lo}$ has increased compared with Puv4, which is also present in the computations. The computed $H_{rms,lo}$ at P5, P4 and P3 shows strong similarity with measurements. The low frequency wave heights reach their overall maximum of approximately 1 m at P2 during the peak of the storm on yearday 122. At this location strong variation in both the computed and measured $H_{rms,lo}$ occurs due to drying and flooding of the instrument at the beginning of the experiment. Overall the comparisons of computed $H_{rms,lo}$ with

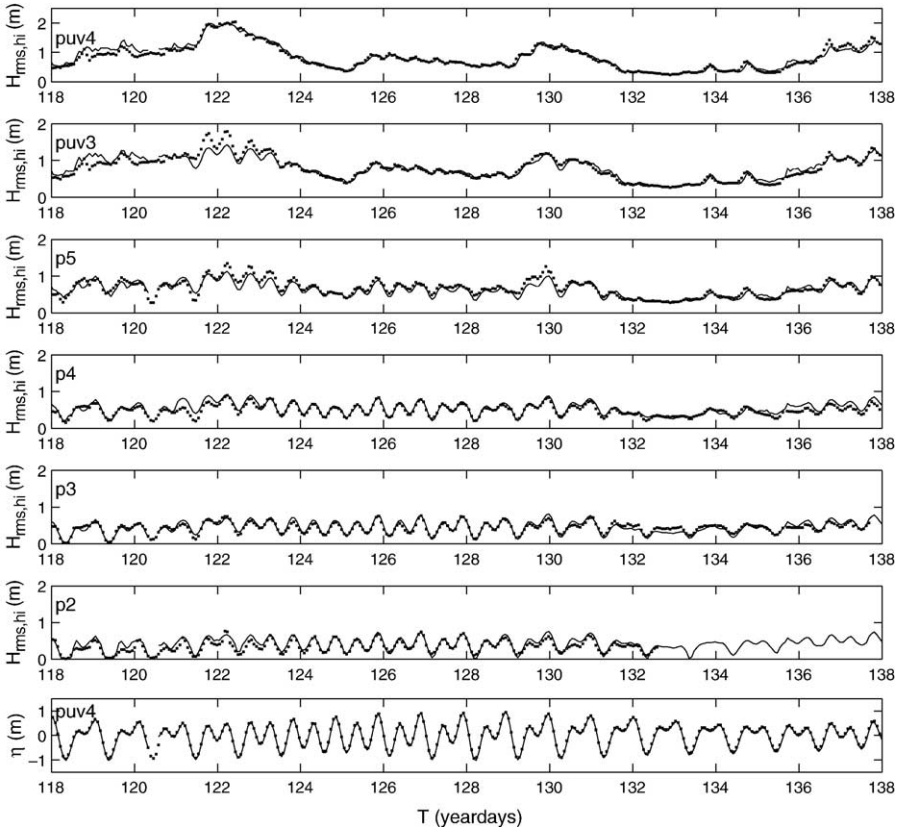

Fig. 3. Measured (squares) and computed (solid lines) incident root-mean-square wave height transformation across the shoal array going from offshore (Puv4) to onshore (P2). Bottom panel: tidal elevation measured (squares) and computed (solid) at Puv4 (offshore) given as a reference.

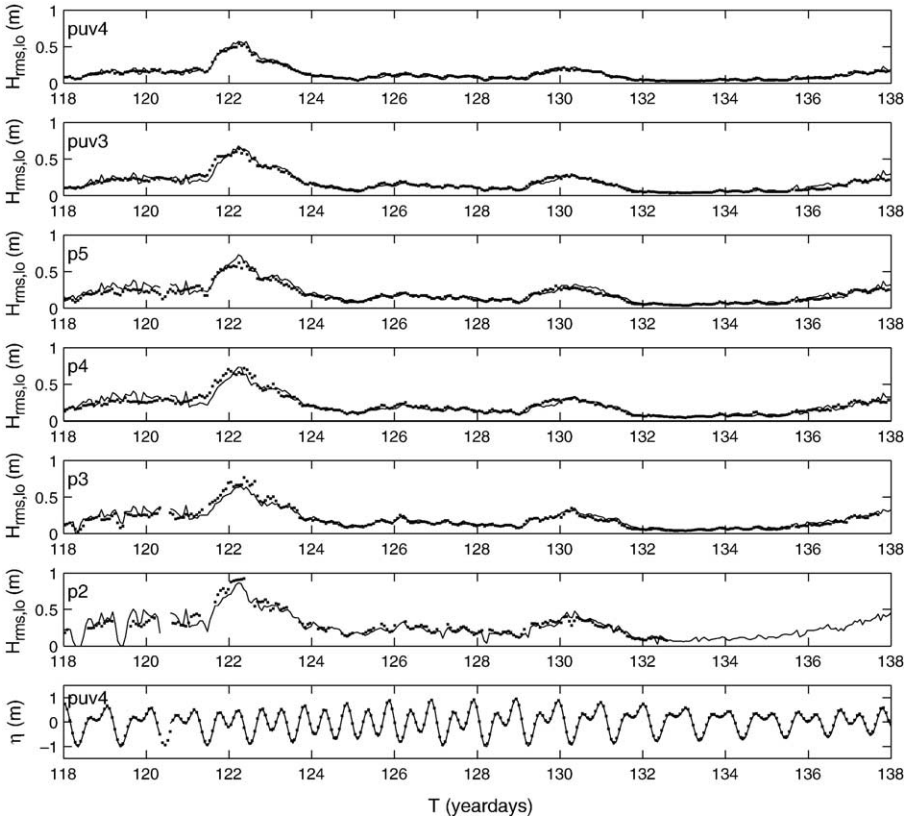

Fig. 4. Measured (squares) and computed (solid lines) 90 min root-mean-square infragravity wave height transformation across the shoal array going from offshore (Puv4) to onshore (P2). Bottom panel: tidal elevation measured (squares) and computed (solid) at Puv4 (offshore) given as a reference.

the measurements show a mean error of $O(4)$ cm with a skill of 0.83 and a regression coefficient of 0.98 (see Table 1).

In contrast to $H_{rms,hi}$, the $H_{rms,lo}$ shows little tidal variation in both measurements and computations in accordance with previous observations (Holman, 1981; Guza and Thornton, 1985; Lippmann et al., 1999, among others). Note that strong tidal modulation in the observed infragravity surface elevation can be present (Okihiro and Guza, 1995; Ruessink, 1998b).

The mean infragravity wave period, $T_{m01,lo}$, which is potentially important for Harbor resonance and ship motions (Bowers, 1971) is considered next. $T_{m01,lo}$ is affected by the frequency distribution of the infragravity energy density, and is therefore sensitive to the nodal structure of the standing infragravity waves (e.g. Suhayda, 1974; Huntley, 1976; Holman, 1981; Guza and Thornton, 1985, and others). As such, it is expected to vary in the cross-shore. At the most offshore sensor, Puv4, the low frequency wave period, $T_{m01,lo}$, is approximately 50 s. The measured low frequency wave period, $T_{m01,lo}$, modulates with the tide, showing an increase in wave period occurring at low tide, which is also present in the modeled results. At Puv3 and P5, $T_{m01,lo}$ shows significantly less variation with the tide in both computations and measurements. At P4 the tidal modulation increases again followed by strong variability in the computed and observed $T_{m01,lo}$ on both the intra-tidal and inter-tidal time scale (correlated with the offshore wave height (see Fig. 1)) at P3. Moving closer to shore, at P2, the variation in $T_{m01,lo}$ diminishes considerably again. The overall skill is 0.83 with a mean ε_r of 8.4 s (see Table 2).

The position of nodes and anti-nodes in the cross-shore standing infragravity waves are a function of the distance from the measurement locations to the tidally modulated shore line. This is reflected in the average (over the experiment) normalized surface elevation spectra (Herbers et al., 1995) at high and low tides at the various sensor locations (Fig. 6). The most offshore sensor (Puv4) shows relatively little structure in both the infragravity and incident wave bands. Still, the spectral changes in infragravity energy density with the tide are significant, with more energy in the lower frequencies at low tide than at high tide, resulting in a relatively wide range of $T_{m01,lo}$ from high to low tides. The computations show quantitative agreement with the normalized spectra, though

Table 2
Root mean square error estimates, ε_r in (s), skill factors and linear regression coefficient, a, for $T_{m01,lo}$ at the cross-shore array

Sensor	X (m)	Y (m)	ε_r(s)	Skill	a
Puv4	235.5	53.5	7.2	0.85	0.97
Puv3	175.0	56.2	5.3	0.88	0.96
P5	141.6	57.5	7.1	0.84	0.91
P4	106.5	57.0	8.9	0.79	0.86
P3	70.2	56.5	13.8	0.79	0.92
P2	52.1	55.7	8.3	0.83	0.88
Mean			8.4	0.83	0.92

differences for individual frequencies can be significant (e.g. at $f=0.025$ Hz). Proceeding shoreward, the nodal structure becomes more evident (compare Puv3 and P5 in Fig. 6) in both computations and measurements. The variation in $T_{m01,lo}$ becomes less, indicating that node-changes at high and low tide cancel each other out. However, at P4 this is apparently not the case, and an increase in the variation of $T_{m01,lo}$ can be observed. The positions of the computed and measured nodes and anti-nodes generally coincide well at these measurement locations. Moving towards P3, the frequency spectrum starts losing structure again with a small variation in $T_{m01,lo}$. The latter is contrary to the results shown in Fig. 5, however the temporal changes in the bed-level due to erosion/accretion of sand at this location are significant (MacMahan et al., 2005). As a result the position of the node's and anti-nodes varies not only due to the tide but also on a slower time-scale associated with the bathymetric changes. This slow variation smoothens the normalized spectrum resulting in an underprediction for the variation of $T_{m01,lo}$. Closer to shore the spectrum becomes more isotropic (sensor P2 in Fig. 6). The normalized spectrum at this location is reproduced by the model computations.

It is noted that the experiment-averaged normalized spectra combine the effects of changes in both the bathymetry and offshore wave conditions on the generation of infragravity waves. Differences with individual spectra can therefore be significant. Still, the present interest is not so much in the individual behavior of a particular wave condition on a particular bathymetry, but the ability to model the general infragravity characteristics on a variable beach topography, for which a comparison with the normalized spectra is appropriate.

3.3. Alongshore array comparison

To examine the model performance for predicting infragravity motions over an alongshore varying bathymetry, the comparison with measurements at the alongshore array of current velocity meters is considered next (Fig. 7). Unfortunately, all but one of the co-located pressure sensors failed at some time within the 20-day period, so comparisons are made with the infragravity velocities only.

Current meter Puv9 is located at the southerly end of the alongshore array (see Fig. 2), which experienced both rip-channel and shoal morphodynamics during the 20-day period (MacMahan et al., 2005). The overall correspondence with the measurements is good, though significant mismatches occur at the more extreme low tides. The current meters deployed on the shoals (Puv1 and Puv2) were only approximately 0.4 m below mean sea level, thus subject to drying and wetting at low tide at times when the shoal itself is still inundated. This hampers a proper comparison with the model computations, which computes infragravity conditions as long as the shoals are inundated (see for example yeardays 126, 127 and 128 for Puv1 and Puv2). To assess the model performance, the skill-parameters computed for the whole period are compared with the values computed only during times the current meters were inundated (excluding times of low tide from the comparison).

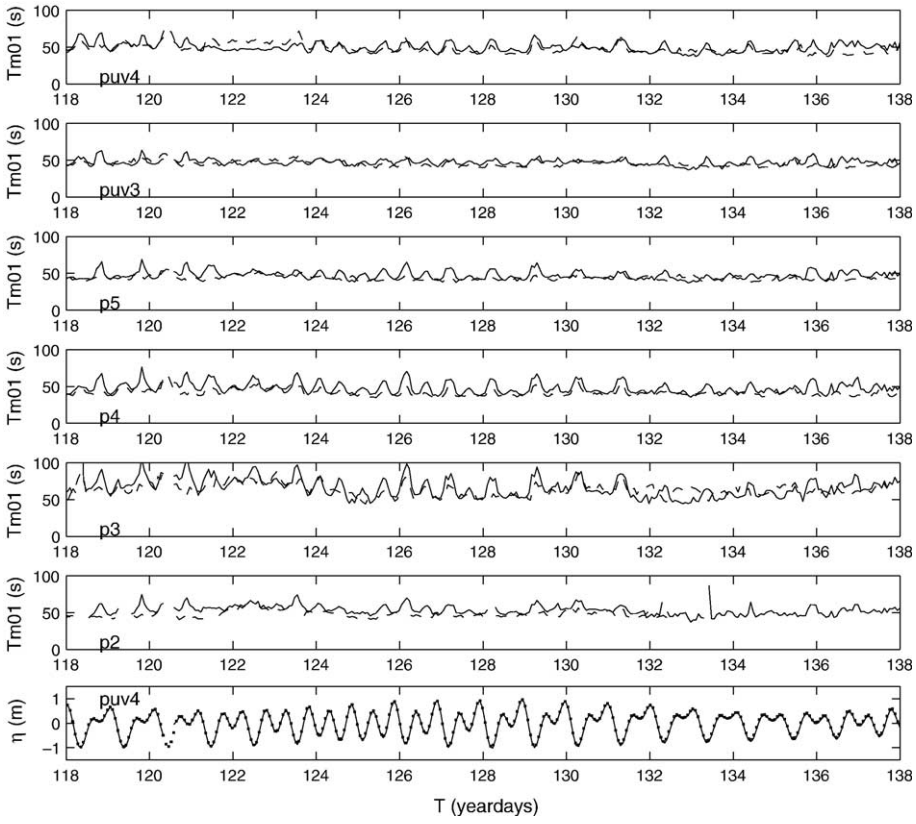

Fig. 5. Measured (dashed) and computed (solid lines) $T_{m01,lo}$ across the shoal array going from offshore (Puv4) to onshore (P2). Bottom panel: tidal elevation measured (squares) and computed (solid) at Puv4 (offshore) given as a reference.

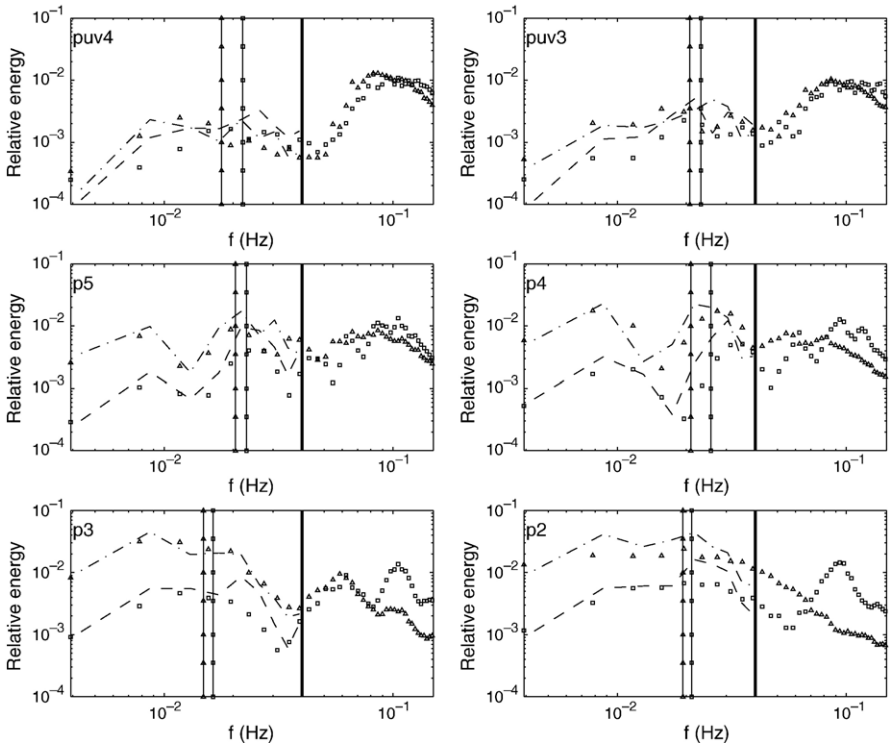

Fig. 6. Average (over the experiment) measured spectra normalized by the total measured energy density at high (squares) and low tides (triangles) with corresponding $T_{m01,lo}^{-1}$ denoted by vertical lines. Average computed spectra normalized by the total measured energy density at high (dashed lines) and low tides (dash-dotted line). Cut-off between low and high frequencies denoted by the thick vertical line at 0.04 Hz.

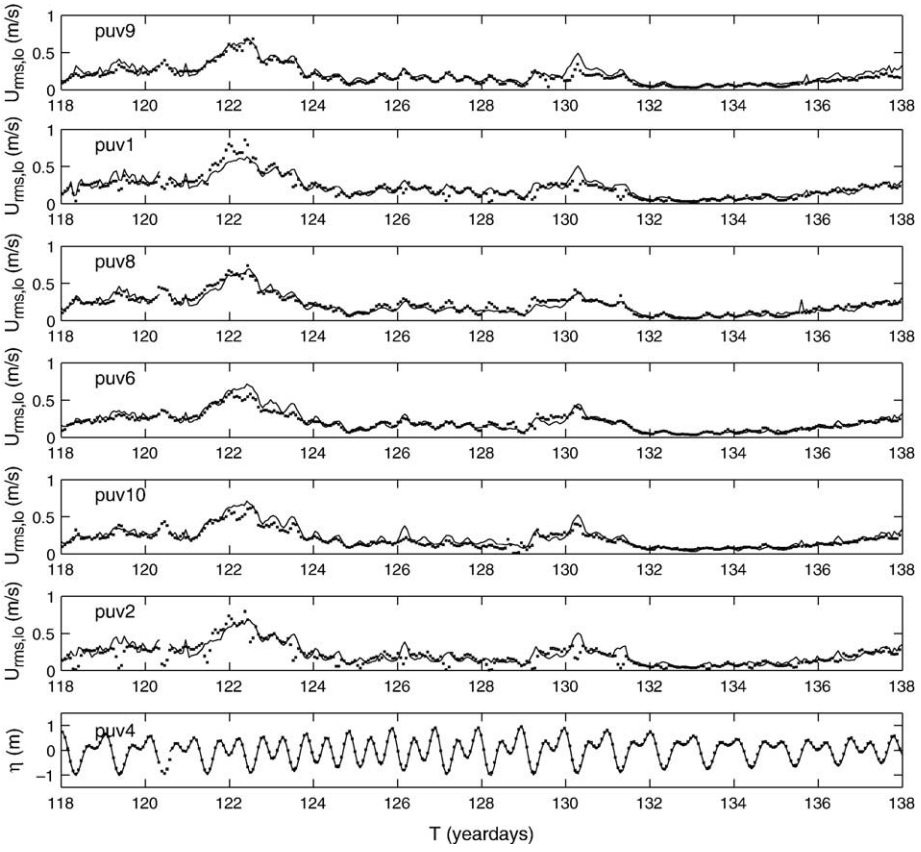

Fig. 7. Measured (squares) and computed (solid lines) $U_{rms,lo}$ at the alongshore array (see Fig. 2 for sensor locations). Bottom panel: tidal elevation measured (squares) and computed (solid) at Puv4 (offshore) given as a reference.

Table 3
Error estimates, ε_r in (m/s), skill factors and linear regression coefficient, a, for cross-shore infragravity velocities at the alongshore array at all tidal elevations (columns 4–6) and tidal levels above MSL only (columns 7–9)

Position	X (m)	Y (m)	ε_r(m/s)	Skill	a	ε_r(m/s)	Skill	a
Puv9	88.9	120.3	0.07	0.77	0.87	0.07	0.74	0.85
Puv1	88.2	57.0	0.10	0.73	0.96	0.06	0.82	1.03
Puv8	88.1	21.7	0.06	0.83	1.01	0.06	0.83	1.01
Puv6	88.0	−3.3	0.07	0.80	0.90	0.06	0.82	0.95
Puv10	83.9	−18.2	0.07	0.79	0.91	0.05	0.82	0.93
Puv2	87.7	−61.9	0.12	0.65	0.89	0.06	0.82	1.07
Mean			0.08	0.76	0.92	0.06	0.81	0.97

Table 4
Error estimates, ε_r in (m/s), skill factors and linear regression coefficient, a, for along-shore infragravity velocities at the alongshore array at all tidal elevations (columns 2–5) and tidal levels above MSL only (columns 6–8)

Instrument	X (m)	Y (m)	ε_r(m/s)	Skill	a	ε_r(m/s)	Skill	a
Puv9	88.9	120.3	0.08	0.55	0.75	0.08	0.44	0.72
Puv1	88.2	57.0	0.06	0.67	0.81	0.06	0.68	0.89
Puv8	88.1	21.7	0.08	0.65	0.88	0.07	0.61	0.99
Puv6	88.0	−3.3	0.06	0.69	0.87	0.05	0.66	0.90
Puv10	83.9	−18.2	0.05	0.70	0.91	0.05	0.67	0.90
Puv2	87.7	−61.9	0.06	0.65	0.85	0.06	0.67	0.85
Mean			0.06	0.65	0.84	0.06	0.62	0.87

This leads to a considerable improvement in the model-skill going from 0.73 to 0.84 and 0.65 to 0.82 (see Table 3) statistically significant at the 5% confidence level. Current meters Puv8, Puv6 and Puv10 were deployed relatively close to each other spanning the width of the rip-channel that was present at yearday 117 (see Fig. 2). Their infragravity response for the 24 days considered is quite similar, and model computations compare favorably with skill factors in the order of 0.80. The overall correspondence (at high tide) of the computed cross-shore infragravity velocity $U_{rms,lo}$ with the measurements is expressed by a mean error of $O(6)$ cm/s, a corresponding skill factor of 0.81 and a regression coefficient of 0.97 (see Table 3). Most of the computations are biased high, as can be inferred from the linear regression coefficients for the individual sensor locations in Table 3.

The alongshore infragravity velocity component, $V_{rms,lo}$, represents obliquely propagating infragravity waves and edge waves. Although the alongshore infragravity velocities are significantly smaller than its cross-shore counterpart, they are not negligible (Fig. 8, note the difference in scale compared with Fig. 7). Discrepancies between computations and measurements are largest at Puv9 and Puv8 during the first storm (yearday 120–122). The comparison at the other sensors is better, though discrepancies still mostly occur during the first storm. The relative spatial variation in both computed and measured infragravity response is stronger than for the cross-shore infragravity velocities. The overall error (at high tide conditions) in the computations is $O(6)$ cm/s with a skill factor of 0.62 and a linear regression coefficient of 0.87 (see Table 4).

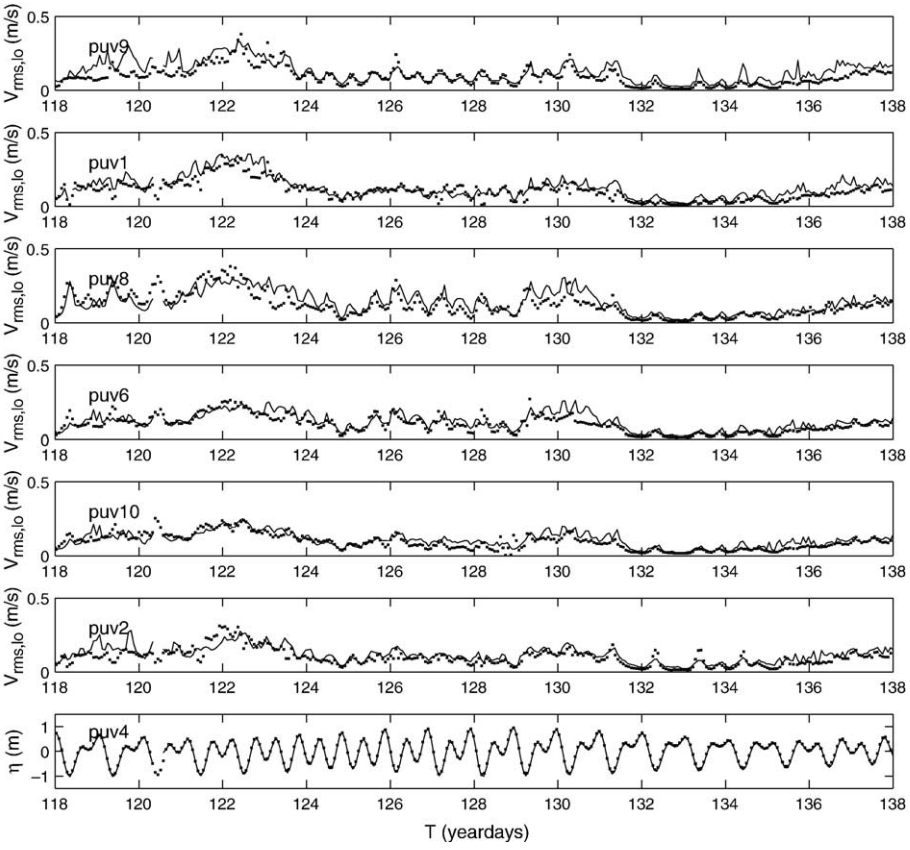

Fig. 8. Measured (squares) and computed (solid lines) $V_{rms,lo}$ at the alongshore array (see Fig. 2 for sensor locations). Bottom panel: tidal elevation measured (squares) and computed (solid) at Puv4 (offshore) given as a reference.

The computed normalized spectra of the cross-shore velocity show more structure than the measurements with more (less) energetic anti-nodes (nodes), though the positions of the computed nodes and anti-nodes show reasonable agreement with the measurements (Fig. 9). Given the fact that the distance from the beach is approximately the same for all instruments, the nodes and anti-nodes occur at similar frequency bandwidths. The agreement for the lower frequencies ($f<0.02$ Hz) is typically better than for frequencies higher than 0.02 Hz. Overall, the energy density for the cross-shore velocities is overpredicted (corresponding to the results presented in Fig. 7).

There is little evidence of alongshore nodal structure in the alongshore velocity energy density spectra at the infragravity frequencies in both measurements and computations at any of the locations (Fig. 9). This suggests that there is no dominant coupling between the alongshore quasi-periodic bathymetry and the infragravity motions during the course of the experiment. Computed results generally agree well with the measurements throughout the infragravity frequency band. The energy density for the alongshore infragravity velocity is typically larger than that of the incident wave band (up to 10 times for the lowest frequencies). The increased contribution of the alongshore infragravity velocities with decreasing frequency may be explained by the increased directional spreading of the infragravity waves forced by the directionally spread incident waves (Herbers et al., 1995), where two swell components of different frequency and direction force an infragravity wave. The directional properties of the resulting infragravity wave depend on the difference wave number of the two swell components. In the case the difference frequency between the two swell components is relatively large, the difference wave number is close to the wave number of the shortest swell component, resulting in an infragravity wave propagating in the direction of this component. As the difference frequency decreases the difference wave number becomes also small, and the infragravity wave can travel at large angles with respect to the two incident swell components. This results in an increased directional spreading of the infragravity waves for decreasing difference frequencies, hence the relative contribution of the alongshore infragravity velocity to the total infragravity motions is expected to increase for decreasing difference frequencies.

4. Discussion

In spite of the strong bathymetric variation (Fig. 2), the infragravity velocities at the alongshore array show remarkably little spatial variation in both computations and measurements (Figs. 7 and 8). In the case of strong coupling between edge waves and quasi-periodic bathymetry, significant spatial variation of infragravity energy is expected, favoring combinations of standing edge waves with alongshore length scales comparable to length scales of the underlying bed-features (Holman and Bowen, 1982; Wright et al., 1982; Chen and Guza, 1998, 1999).

In the following, the coupling is quantified by examining the spatial variation of the total infragravity motion at the

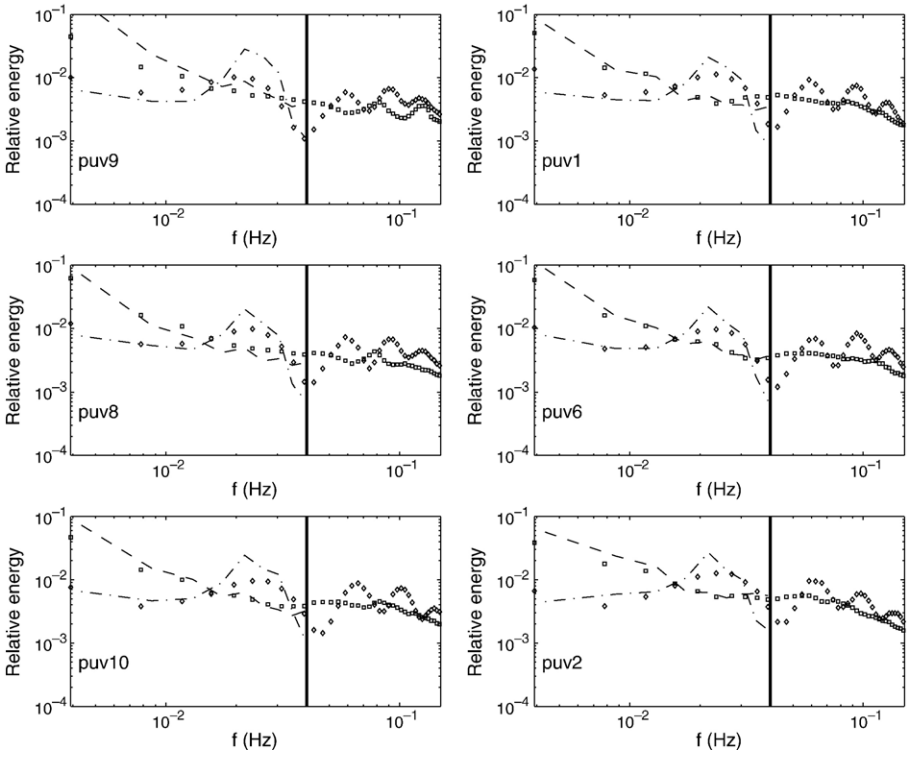

Fig. 9. Averaged (over the experiment) measured spectra at the alongshore array normalized by the measured total energy density of the cross-shore velocities (diamonds) and alongshore velocities (squares) during times of inundation. Average computed spectra normalized by the measured total energy density of the cross-shore velocities (dash-dotted lines) and alongshore velocities (dashed line). Low frequency cut-off denoted by the thick vertical line at 0.04 Hz.

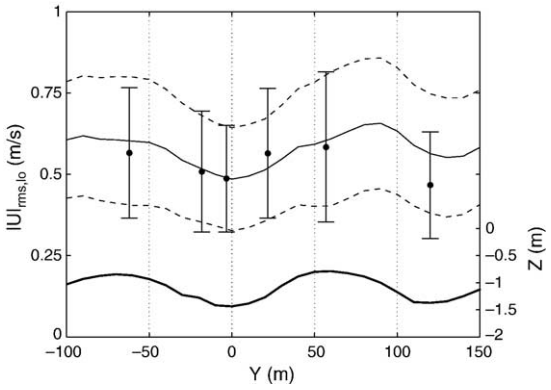

Fig. 10. Computed daily averaged $|U|_{\mathrm{rms,lo}}$ for yearday 121 (solid line) plus or minus the standard deviation (dashed lines) at the alongshore array compared with the measured daily averaged $|U|_{\mathrm{rms,lo}}$ (dots) plus or minus its standard deviation (vertical lines). Bottom profile along the alongshore array (thick solid line) given as a reference.

alongshore array, given by:

$$|U|_{\mathrm{rms,lo}} = \sqrt{U^2_{\mathrm{rms,lo}} + V^2_{\mathrm{rms,lo}}}. \tag{5}$$

Calculating the daily mean and standard deviation of 48 half-hour estimates of the total infragravity motions for both computations and measurements on yearday 121 shows that computed alongshore variation in $|U|_{\mathrm{rms,lo}}$ compares well with the measurements (Fig. 10). This holds for the mean and the standard deviation of $|U|_{\mathrm{rms,lo}}$. The mild alongshore changes of both measured and computed infragravity velocities coincide with changes in the underlying alongshore depth profile, where $|U|_{\mathrm{rms,lo}}$ within the rip-channels is typically less than on the neighboring shoals. This is consistent with predominantly cross-shore standing infragravity motions (MacMahan et al., 2004a) and strong coupling is apparently not present during this period of time.

The apparent absence in strong coupling between the edge wave field and the quasi-periodic bathymetry is examined in more detail. Performing an FFT on the alongshore bathymetry for yearday 130 (left panel of Fig. 11) within the nearshore (50 m$<X<$220 m) shows a number of clear peaks both offshore, at $k_y = O(0.002)$ m^{-1}, at the outer surfzone around $X = 130$ m with $k_y = O(0.011)$ m^{-1} corresponding to the rip-channel spacing, and a number of peaks of different alongshore wave numbers closer to shore associated with the shore-connected shoals (right panel of Fig. 11). In the following, calculated alongshore infragravity velocity $f-k_y$-spectra for that time are examined for amplification at length scales similar to the alongshore spacing in the bathymetry.

Velocity $f-k_y$-spectra are calculated from 8 consecutive 30 min time series of the alongshore current velocity starting on yearday 130, hour 15 (tidal elevation remained approximately at MSL during the 4-h period), along alongshore transects resulting in a frequency resolution of 0.00056 Hz and wave number resolution of 0.001 m^{-1} with 16 degrees of freedom. Theoretical edge wave dispersion curves are given as a reference, and are obtained from the edge wave dispersion relation on a plane beach (Eckart, 1951):

$$\omega = \sqrt{g k_y (2n+1)\tan m} \tag{6}$$

where n is the edge wave mode number and m represents the beach slope. Fitting the dispersion curves to the computed edge wave modes results in a beach slope of 1/22 for the zero mode edge waves (which experience the steeper slope close to the shore) and $m = 1/30$ for the first mode edge waves (which have a larger cross-shore extend thus also experiencing the milder slope of the shoal).

Close to the shore, at $X = 68$ m, the energy density follows the zero mode dispersion lines, however the scatter around these curves is significant. In addition, there are $f-k_y$ combinations that appear more energetic than others. This is apparent at $f = O(0.025)$ Hz and $k_y = +/- O(0.009)$ m^{-1} (upper arrow in left panel of Fig. 12) and $f = O(0.015)$ Hz and $k_y = +/- O(0.004)$ m^{-1} (lower arrow in left panel of Fig. 12). Relatively high energy density levels are also observed at frequencies lower than 0.01 Hz with $|k_y| < 0.002$ m^{-1}.

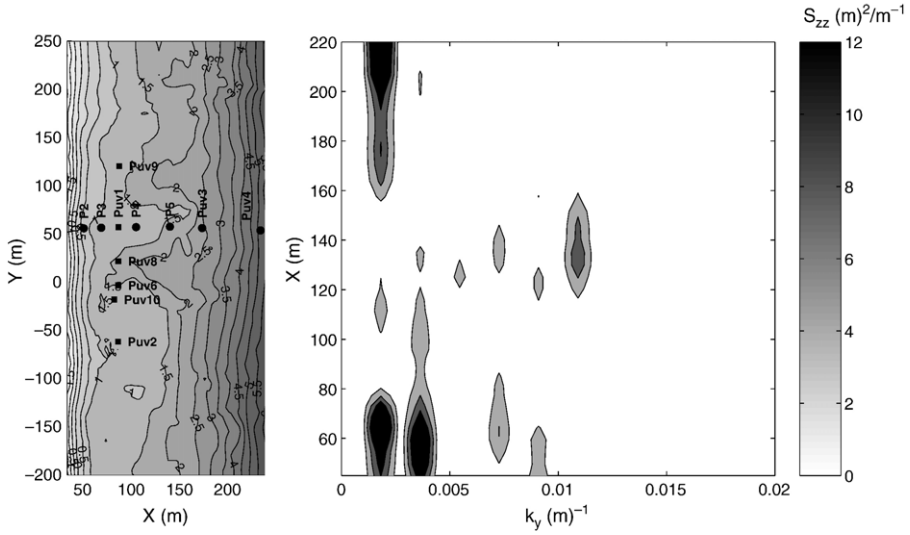

Fig. 11. Left panel: survey for yearday 131. Right panel: cross-shore distribution of alongshore bed-elevation spectra.

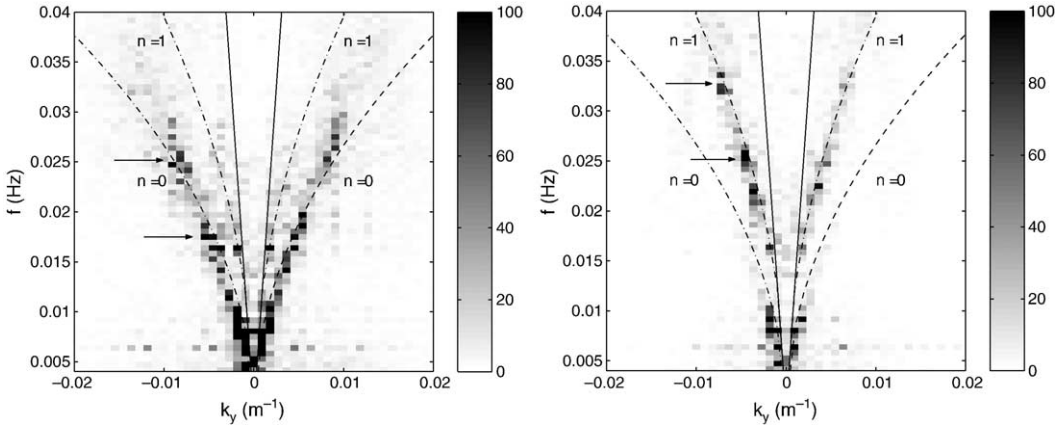

Fig. 12. $f-k_y$-spectra of computed v for yearday 130, hour 15. Left panel: at $X=68$ m (near the shore line). Right panel: at $X=146$ m (outer edge of the surfzone).

Further offshore, at $x=146$ m, the energy density is predominantly distributed along the first mode edge wave curve (right panel of Fig. 12). Energy density is concentrated around $f=O(0.032)$ Hz and $k_y=+/-O(0.007)$ m^{-1} (upper arrow in right panel of Fig. 12) and around $f=O(0.025)$ Hz and $k_y=+/-O(0.004)$ m^{-1} (lower arrow in right panel of Fig. 12) and also for the lower frequencies around $f=O(0.01)$ Hz and $k_y=+/-O(0.002)$ m^{-1}. In contrast to the $f-k_y$-spectrum near the shore line the offshore spectrum displays a bias with larger energy density for the negative alongshore wave numbers.

To discriminate between the amplification of edge wave modes coupled to the quasi-periodic bathymetry and preferential forcing of edge–wave modes by the directionally spread wave groups, these spectra are compared with $f-k_y$-spectra calculated for an alongshore averaged uniform bathymetry. To that end the computed alongshore velocity spectra are summed over all frequencies, i.e. mapping the spectral densities onto the k_y-plane. This procedure is performed for all cross-shore locations within the nearshore (50 m$<X<$220 m) resulting in a cross-shore distribution of the frequency integrated alongshore infragravity spectra both for the actual bathymetry and the alongshore averaged bathymetry. Amplification is then determined by the ratio of the two spectra:

$$A(x,k_y)=\frac{\int_{0.004\mathrm{Hz}}^{0.04\mathrm{Hz}} S_{vv}(x,f,k_y)\,df}{\max\left(\epsilon,\int_{0.004\mathrm{Hz}}^{0.04\mathrm{Hz}} \bar{S}_{vv}(x,f,k_y)\,df\right)} \tag{7}$$

where $\bar{S}_{vv}$ represents the spectral density for the alongshore infragravity velocity on the alongshore uniform beach and ϵ is a threshold set at 0.1 $(m/s)^2/m^{-1}$ to avoid the amplification of noise. The strongest amplification occurs close to shore (Fig. 13) at length scales that are also present in the alongshore bathymetry, most notably at $k_y=+/-0.009$ m^{-1}, at $k_y=+/-0.0035$ m^{-1} and at their difference wave number $k_y=+/-0.0055$ m^{-1}, that is not present in the shore-line bathymetry (right panel of Fig. 11), suggesting an edge–wave interaction. The amplification drops off with increasing offshore distance with a minimum located around $X=90$ m

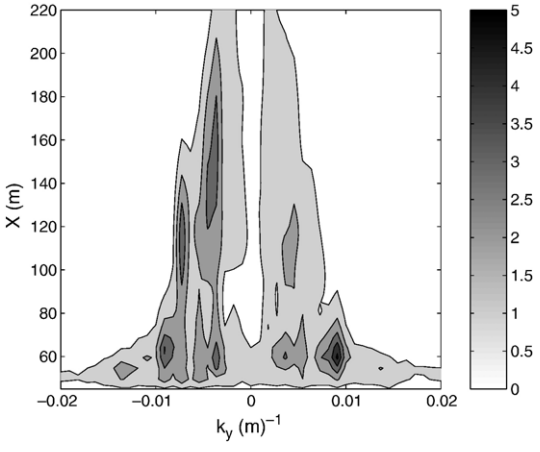

Fig. 13. Cross-shore distribution of amplification, A, of frequency-integrated alongshore infragravity velocity energy density with respect to the alongshore uniform bathymetry. First contour interval at amplification of 1.

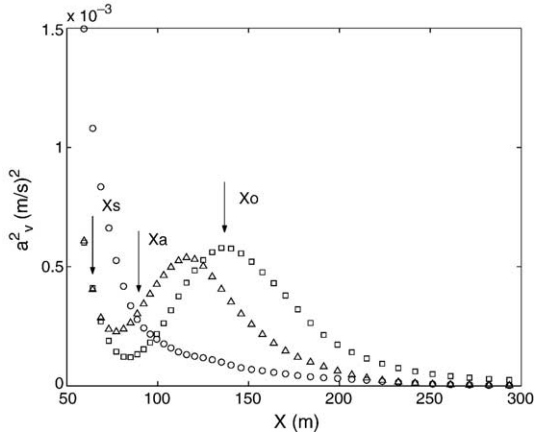

Fig. 14. Cross-shore distribution of alongshore velocity amplitude squared of computed zero mode edge waves (circles) at 0.024 Hz$<f<$0.028 Hz and 0.006 $m^{-1}<|k_y|<0.011$ m^{-1} (corresponding to upper arrow in the upper left panel of Fig. 12). Similar for the first mode edge waves (triangles) at 0.030 Hz$<f<$0.034 Hz and 0.006 $m^{-1}<|k_y|<0.011$ m^{-1} (upper arrow in lower left panel of Fig. 12) and first mode edge waves at 0.022 Hz$<f<$0.026 Hz and 0.003 $m^{-1}<|k_y|<0.006$ m^{-1} (lower arrow in lower left panel of Fig. 12) for yearday 130, hour 15. X_s denotes the virtual alongshore array at $X=68$ m, X_a denotes cross-shore position of the alongshore array at $X=88$ m and X_o denotes the position of the virtual offshore alongshore array at $X=146$ m.

corresponding to the position of the alongshore measurement array. Offshore of the alongshore array the amplification increases again with maxima located around $X=130$ m.

The observed local minimum in the amplification is a result of the fact that the alongshore measurement array is located close to the node in the first mode edge waves and too far seaward for the zero mode edge waves to be of much significance as can be inferred from the cross-shore distribution of the zero and first mode edge waves at which the energy density is concentrated (Fig. 14).

Amplification at the scale of the rip-channel spacing $k_y=0.011$ m^{-1} at the outer surfzone around $X=130$ m (right panel of Fig. 11) is not present in the alongshore infragravity velocity response (Fig. 13). This absence of amplification is also associated with the cross-shore structure of the edge waves. The edge wave dispersion curves show that only the zero-mode edge wave can contribute to the energy density at $k_y=0.011$ m^{-1} (left panel of Fig. 12). All other modes have longer wave lengths (smaller k_y) at the infragravity frequencies. However, the zero mode edge wave has most of its energy close to the shore line (Fig. 14) and is strongly reduced at $X=130$ m. Consequently, the response of this mode is governed by the bathymetry close to the shore and not by the alongshore bathymetry around $X=130$ m, i.e. amplification at the alongshore rip-spacing is not observed. Apparently the alongshore separation distance of the rip-channels at this location is too short for significant edge–wave coupling to occur during this time. Amplification at longer spatial scales, corresponding to smaller k_y values, does occur around $X=130$ m. However, these length scales are dominant at the shore line bathymetry (right panel of Fig. 11) and not at $X=130$ m. This suggests that these motions are also governed by the bathymetry close to the shoreline and what is observed are the anti-nodes of the higher mode edge–waves (Fig. 14).

In summary, the $f-k_y$-analysis shows preferential amplification at $f-k_y$ combinations which have similar length scales as the underlying bathymetry. This suggests that there is a coupling between edge waves and the underlying quasi-periodic bathymetry, resulting in a significant increase, up to a factor of five, in alongshore velocity energy density compared with the case of edge waves on an alongshore averaged uniform bathymetry. Still, the overall coupling between the total infragravity motion, $|U|_{\mathrm{rms,lo}}$, and the quasi-periodic bathymetry is relatively weak, given the fact that cross-shore motions dominate the infragravity wave field. The predominance of the cross-shore infragravity motions is associated with the persistent normally incident swell (see Fig. 1).

5. Conclusions

Computational output of a two-dimensional wave and flow model operating on the time-scale of wave groups has been compared with detailed measurements of infragravity conditions obtained during the RIPEX-SBE field experiment at Monterey Bay. The overall performance of the present model approach compared with measurements at both the cross-shore and alongshore array are satisfactory, typically explaining up to 80% of the infragravity wave height and 70% of the infragravity velocities present.

In addition, the average (over the experiment) normalized infragravity surface elevation and velocity spectra are reproduced by the model. The infragravity wave period is also well predicted in both time and space.

Both computations and measurements show relatively little variation in infragravity intensity in the alongshore, even though the underlying bathymetry is strongly variable. A more detailed analysis of the model computations shows that coupling between the edge wave field and underlying quasi-periodic bathymetry is present. However, given the predominance of cross-shore infragravity motions forced by near-normally incident sea-swell waves, the coupling is only weak for the total infragravity motion. Hence the small alongshore variability in the computed infragravity conditions is consistent with observations.

The predictive capability of the model for the infragravity motions throughout the experiment is relatively high, expressed by the model skill, even though differences between the actual bathymetry and the computational bathymetry are expected to be significant (i.e. given the observed differences between the individual surveys by MacMahan et al. (2005)). This consistent high skill is positively influenced by the relatively weak coupling, where differences between the actual and computed bathymetry only modestly affect the infragravity motions. This high skill is not expected to hold for the modelling of the mean flows which are more susceptible to small changes in the bathymetry.

Acknowledgements

We thank Tom Herbers and Paul Jessen for providing us with the offshore bouy data, Edie Gallagher and Maggie for the instrument surveys and general support, Tom Lippman, Mark Orzech, Bruce Morris, Rob Wyland, Jim Stockel, Ron Cowen, Benji, Jason Engle, Greg Miller, Loraine Chial, Charlotte Welsch, Denis Morichon, Fabrice Ardhuin, Jennifer Shore and the Hopkins Marine Station volunteers for their contributions in performing in the RIPEX-SBE experiment. The Steep Beach Experiment and EBT and TPS were funded by the Office of Naval Research, Coastal Science Program, under contract N00014-01-WR-20023. JM was funded by the Florida Sea Grant Program. Part of the work presented here was done while AR held a National Research Council-NPS Research Associateship funded through the National Ocean Partnership Program (NOPP) under contract N0001463WR20191 and the Office of Naval Research under contract N00014-01-WR20023. Part of this material is based upon work funded by the National Science Foundation under grant 0136882. Additional funding from the Dutch National Science Foundation, contract DCB.5856 is much appreciated. We thank WL Delft-Hydraulics for the use of their Delft3D software. Ad Reniers thanks Jurjen Battjes for his inspiration, guidance and friendship.

References

Bowen, A.J., Inman, D.I., 1971. Edge waves and crescentic bars. J. Geophys. Res. 76, 8662–8671.

Bowers, E.C., 1971. Harbour resonance due to set-down beneath wave groups. J. Fluid Mech. 79, 71–79.

Chen, Y., Guza, R.T., 1998. Resonant scattering of edge waves by longshore periodic topography. J. Fluid Mech. 369, 91–123.

Chen, Y., Guza, R.T., 1999. Resonant scattering of edge waves by longshore periodic topography: finite beach slope. J. Fluid Mech. 387, 255–269.

Eckart, C., 1951. Surface waves on water of variable depth, Wave Rep. 100, Scripps Institution of Oceanography, University of California, La Jolla.

Elgar, S., Herbers, T.H.C., Okihiro, M., Oltman-Shay, J., Guza, R.T., 1992. Observations of infragravity waves. J. Geophys. Res. 97, 15,573–15,577.

Fredsoe, J., 1984. Turbulent boundary layers in wave-current motion. J. Hydraulic Eng. American Society of Civil Engineers, New York, pp. 1103–1120.

Gallagher, E.L., Elgar, S., Guza, R.T., 1998. Observations of sand bar evolution on a natural beach. J. Geophys. Res. 103, 3203–3215.

Guza, R.T., Thornton, E.B., 1985. Observations of surf beat. J. Geophys. Res. 90, 3161–3171.

Herbers, T.H.C., Elgar, S., Guza, R.T., 1995. Generation and propagation of infragravity waves. J. Geophys. Res. 100, 24,863–24,872.

Holman, R.A., 1981. Infragravity energy in the surfzone. J. Geophys. Res. 86, 6442–6450.

Holman, R.A., Bowen, A.J., 1982. Bars, bumps and holes: models for the generation of complex beach topography. J. Geophys. Res. 87, 457–468.

Huntley, D.A., 1976. Long-period waves on a natural beach. J. Geophys. Res. 36, 6441–6449.

Huntley, D.A., Guza, R.T., Thornton, E.B., 1981. Field observations of surf beat: Part I. Progressive edge waves. J. Geophys. Res. 86, 6451–6466.

Lippmann, T.C., Herbers, T.H.C., Thornton, E.B., 1999. Gravity and shear wave contributions to nearshore infragravity motions. J. Phys. Oceanogr. 29, 231–239.

List, J.H., 1992. A model for the generation of two dimensional surf beat. J. Geophys. Res. 97, 5623–5635.

MacMahan, J.H., Reniers, A.J.H.M., Thornton, E.B., Stanton, T.P., 2004a. Infragravity rip current pulsations. J. Geophys. Res. 109, C01033. doi:10.1029/2003JC002068.

MacMahan, J.H., Reniers, A.J.H.M., Thornton, E.B., Stanton, T.P., 2004b. Surf zone eddies coupled with rip current morphology. J. Geophys. Res. 109, C07004. doi:10.1029/2003JC002083.

MacMahan, J.H., Thornton, E.B., Stanton, T.P., Reniers, A.J.H.M., 2005. RIPEX: observations of a rip current system. Mar. Geol. 218 (1–4).

Munk, W.H., 1949. Surf beats. Trans. Am. Geophys. Union 30, 849–854.

Nairn, R.B., Roelvink, J.A., Southgate, H.N., 1990. Transition zone width and implications for modeling surfzone hydrodynamics. Proceedings of the 22nd International Conference on Coastal Engineering. American Society of Civil Engineers, New York, pp. 68–81.

Okihiro, M., Guza, R.T., 1995. Infragravity energy modulation by tides. J. Geophys. Res. 100, 16,143–16,148.

Okihiro, M., Guza, R.T., Seymour, R.J., 1992. Bound infragravity waves. J. Geophys. Res. 97, 11,453–11,469.

Oltman-Shay, J., Guza, R.T., 1987. Infragravity edge wave observations on two California beaches. J. Phys. Oceanogr. 17, 644–663.

Overton, M.F., Fischer, J.S., 1988. Simulation of modeling dune erosion. Proceedings of the 21st International Conference on Coastal Engineering. American Society of Civil Engineers, New York, pp. 1857–1867.

Reniers, A.J.H.M, Van Dongeren, A.R., Battjes, J.A., Thornton, E.B., 2002. Linear modeling of infragravity waves during Delilah. J. Geophys. Res. 107 (C10), 3137. doi:10.1029/2002JC001586.

Reniers, A.J.H.M, Roelvink, J.A., Thornton, E.B., 2004. Morphodynamic modeling of an embayed beach under wave group forcing. J. Geophys. Res. 109, C01030.

Roelvink, J.A., 1993. Dissipation in random wave groups incident on a beach. Coast. Eng. 19, 127–150.

Ruessink, B.G., 1998a. Bound and free infragravity waves in the nearshore zone under breaking and nonbreaking conditions. J. Geophys. Res. 103, 12,795–12,805.

Ruessink, B.G., 1998b. The temporal and spatial variability of infragravity energy in a barred nearshore zone. Cont. Shelf Res. 18, 585–605.

Soulsby, R.L., Hamm, L., Klopman, G., Myrhaug, D., Simons, R.R., Thomas, G.P., 1993. Wave-current interaction within and outside the bottom boundary layer. Coast. Eng. 21, 41–69.

Stelling, G.S., Wiersma, A.K., Willemse, J.B.T.M., 1986. Practical Aspects of Accurate Tidal Computations. J. of Hydraulics Engineering. American Society of Civil Engineers, New York.

Suhayda, J.N., 1974. Standing waves on beaches. J. Geophys. Res. 79, 3065–3071.

Swart, D.H., 1974. Offshore Sediment Transport and Equilibrium Beach Profiles. Delft Hydraulics Report, Publ, vol. 131. WL-Delft Hydraulics, Delft, The Netherlands.

Thornton, E.B., Kim, C.S., 1993. Longshore current and wave height modulation at tidal frequency inside the surfzone. J. Geophys. Res. 98, 16,509–16,519.

Tucker, M.J., 1950. Surf beats: sea waves of 1 to 5 min period. Proc. R. Soc. Lond., A, 565–573.

Van Dongeren, A.R., Reniers, A.J.H.M., Battjes, J.A., Svendsen, I.A., 2003. Numerical modeling of infragravity wave response during Delilah. J. Geophys. Res. 108 (C9), 3288. doi:10.1029/2002JC001586.

Van Gent, M.R.A., 2001. Wave runup on dikes with shallow foreshores. J. Waterw. Port Coast. Ocean Eng. 127 (5), 254–262.

Verboom, G.K., Slob, A., 1984. Weakly reflective boundary conditions for two-dimensional water flow problems. Proceedings 5th International Conference on Finite Elements in Water Resources.

Wright, L.D., Chappell, J., Thom, B.G., Bradshaw, M.P., Cowell, P., 1979. Morphodynamics of reflective and dissipative beaches and inshore systems: southeastern Australia. Mar. Geol. 32.

Wright, L.D., Guza, R.T., Short, A.D., 1982. Dynamics of a high energy dissipative surf-zone. Mar. Geol. 45, 41–62.